Research paper

Exploring the influence of water film thickness on the yield stress of cement-limestone pastes: a comprehensive analysis

Qian Zhang[1]

Abstract: This study delves into the influence of water film thickness (WFT) on the rheological characteristics, particularly the yield stress, of cement paste incorporating limestone powder. Employing an Anton Paar MCR 102 rheometer, precise measurements of both the static and dynamic yield stress were conducted. Artificial neural networks (ANN) were then applied to explore the relationship between WFT and yield stresses. The findings reveal an approximate linear growth pattern in the shear stress-shear rate profile of cement-limestone paste, with an intensified shear thickening observed as limestone powder content increases. The augmentation of limestone powder and specific surface area notably enhances both static and dynamic yield stresses, with the latter reaching 70.26 Pa in the case of a paste containing 50% Class III limestone powder (1088 m^2/kg). The WFT of cement-limestone paste particles is contingent on the ratio of solid particle packing density to total specific surface area, exhibiting an increase with rising solid particle packing density. Both static and dynamic yield stresses exhibit a negative correlation with WFT. Artificial neural networks demonstrate efficacy in predicting static and dynamic yield stresses based on mix ratio parameters and WFT, with a higher prediction accuracy for static yield stress, reflected in an R^2 value of 0.9745.

Keywords: Portland cement, limestone powder, water film thickness, yield stress, artificial neural network

[1]MSc. Eng., Department of Civil Engineering, Changzhi Vocational and Technical College, Changzhi 046000, China, e-mail: 1157756861@qq.com, ORCID: 0009-0004-0564-868X

1. Introduction

Fresh cement paste constitutes a sophisticated multiphase suspension system [1]. Owing to ongoing hydration processes, the rheological attributes of the cement paste are dynamic, exhibiting alterations over time, notably characterized by an increase in parameters such as yield stress and viscosity [2–6]. Preliminary to the onset of initial setting, a rheometer can be employed to assess the rheological properties of the cement paste. The yield stress is typically categorized into dynamic and static components [7, 8]. The former denotes the stress required to sustain the paste in a flowing state, while the latter signifies the minimum stress necessary for transitioning the paste from a static to a flowing state. In concert with the burgeoning field of 3D printing technology, it is underscored that the paste must possess commendable static and dynamic yield stresses [9, 10]. Static yield stress ensures the paste's resilience against pressure from the superimposed layers post-extrusion, preventing deformation. Simultaneously, dynamic yield stress is pivotal in averting paste blockages during transportation, especially through pumping. Excessive dynamic yield stress could lead to heightened stress requirements for maintaining paste flow, potentially causing local paste adhesion to the pipeline's inner surface, thereby impeding pumping efficiency [11–13].

To quantify the yield stress of cementitious materials, two predominant testing methodologies are commonly employed: one involves utilizing flow curves and specific rheological models for fitting rheological parameters, while the other entails applying a constant low shear rate through an external force to measure the stress peak of the paste [14–16]. Beyond flow characteristics, the viscoelasticity of freshly mixed paste holds significance. Viscoelasticity, distinguished from flow testing, necessitates applying alternating stress to the paste and recording parameters such as storage modulus (G'), loss modulus (G''), and phase angle during oscillation [17, 18]. These parameters facilitate the analysis of whether the paste predominantly exhibits viscous or elastic behavior at a given moment. The elastic modulus further characterizes the extent of paste deformation under external forces and its recovery after force removal. Rooted in the cement hydration mechanism, the yield stress and viscoelastic properties of the slurry hinge upon the interplay between colloidal particles and the overlapping effects of C–S–H bridges engendered by hydration [3, 19, 20]. A profound understanding of these properties offers crucial insights for comprehending the early performance of cement slurries.

Cement, a globally ubiquitous building material, serves as a binder in concrete systems, effectively uniting coarse aggregates, fine aggregates, and other components into a cohesive whole, ensuring the overall multiphase system possesses sufficient strength for engineering applications. While Portland cement (PC) remains the predominant clinker in use, its production contributes significantly to carbon emissions [21–24]. The calcination of limestone in the cement manufacturing process releases carbon dioxide, and this process entails substantial energy consumption. Studies indicate that carbon emissions associated with cement production constitute 6–8% of the world's total anthropogenic carbon emissions, a substantial environmental concern [25–27]. Consequently, scholars advocate exploring alternative supplementary cementitious materials to mitigate cement consumption. Limestone powder, a representative supplementary material, enhances the particle size distribution of the overall system, enabling finer particles to fill the interstices among coarser particles [28–30]. This reduces the need for

water to fill pores, as excess water can envelop particle surfaces, forming a lubricating film that facilitates particle sliding, thereby enhancing the rheological properties of the paste.

Packing density pertains to the proportion of space occupied by the filling material, a parameter influenced by factors such as particle shape and size distribution [31, 32]. When considering cement, supplementary cementitious materials (SCMs) particles, and flowing water as distinct systems within the paste, the ratio between them significantly impacts paste fluidity. Water in the paste serves distinct functions, categorized into chemically bound water, a product of the cement reaction, and free water, which, in turn, includes filling water and residual water. The quantity of residual water constitutes a crucial parameter affecting paste fluidity, posing a challenge in precise calculation [33–37]. The introduction of the water film thickness theory aims to address these challenges. Incorporating the concept of water film thickness into the analysis of cement paste yield stress offers a clearer and more profound understanding of the paste's rheological properties.

This study involved quantifying particle packing density through standard consistency water consumption, and determining water film thickness based on the aggregate particle surface area. Concurrently, a rheometer was employed to measure both static and dynamic yield stresses in the cement limestone powder paste. Subsequently, contemporary machine learning techniques were applied to analyze the interrelation between water film thickness and yield stress. This endeavor aspires to furnish a theoretical and empirical foundation for a more profound comprehension of the evolution of yield stress in cement limestone powder.

2. Materials and experimental procedure

2.1. Materials and mix proportions

Portland cement (P·I 42.5) is provided by China United Cement Group Co., Ltd. Its specific surface area is 340 m^2/kg. The limestone powder, exhibiting a $CaCO_3$ purity of 99%, was categorized into three specific surface area levels: 389, 756, and 1088 m^2/kg, denoted as L-I, L-II, and L-III. The density of Portland cement is 1.4 g/cm^2, while the densities of the three limestone powders are 2.7 g/cm^3, 2.25 g/cm^3, and 1.98 g/cm^3, respectively. The experimental mix proportions, detailed in Table 1, involved varying the substitution rate of limestone powder from 10% to 50%. Three types of limestone powder with distinct specific surface areas were introduced to investigate the alterations in yield stress within the composite paste under different particle size distributions.

2.2. Testing methods

2.2.1. Rheology

An Anton Paar MCR 102 rheometer was employed to assess the yield stress of the fresh cement-limestone paste. Dynamic yield stress was determined through the flow curve of shear stress-shear rate, while static yield stress was ascertained via the stress growth mode at low shear rates. Initially, the powder and water were weighed according to the mix ratio outlined in

Table 1, followed by rapid mixing using a cement paste mixer for 5 minutes. Subsequently, the resulting paste was placed into the rheometer cylinder for testing, involving a step-up every 5 seconds with a rate increase from 20 s^{-1} to 100 s^{-1}, followed by a decrease in the same manner. This testing protocol, depicted in Fig. 1, spanned a total duration of 45 seconds, with the data utilized for calculating dynamic yield stress obtained from the shear rate decrease segment.

Table 1. Mix proportions of cement-limestone pastes

Sample	Mix proportion (wt.%)		w/b
	PC	Limestone	
P100	100	0	0.4
P90L10-I	90	10	0.4
P80L20-I	80	20	0.4
P70L30-I	70	30	0.4
P60L40-I	60	40	0.4
P50L50-I	50	50	0.4
P90L10-II	90	10	0.4
P80L20-II	80	20	0.4
P70L30-II	70	30	0.4
P60L40-II	60	40	0.4
P50L50-II	50	50	0.4
P90L10-III	90	10	0.4
P80L20-III	80	20	0.4
P70L30-III	70	30	0.4
P60L40-III	60	40	0.4
P50L50-III	50	50	0.4

The rheological behavior of cement-limestone paste was described using a modified Bingham model expressed as Eq. (2.1). Where, τ_0 represents the dynamic yield stress, μ denotes the plastic viscosity (Pa·s), and c stands for the second-order parameter (Pa·s^2) [38].

$$(2.1) \qquad\qquad \tau = \tau_0 + \mu\gamma + c\gamma^2$$

The static yield stress of the composite paste is tested by applying a stress with a shear rate of 0.01 s^{-1}. Each test point was recorded every 5 seconds for a duration of 90 seconds. Due to the rapid increase and then decrease of shear stress during the testing process until it stabilizes, the highest shear stress during the testing process is considered as the static yield stress in that state.
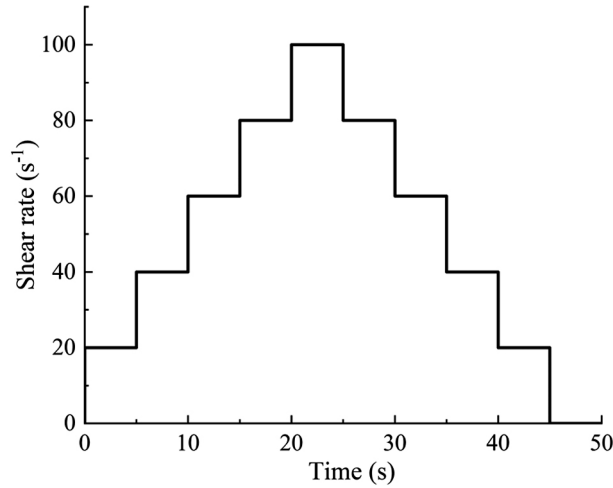
Fig. 1. Test system of rheological measurements

2.2.2. Water film thickness

The determination of the total specific surface area (TSSA) of particles in cement-limestone paste is accomplished through Eq. (2.2), defined as follows [39]:

$$\text{(2.2)} \qquad \text{TSSA} = y_c u_c + y_l u_l$$

where, y_c and y_l represent the specific surface areas of PC and limestone powder, respectively, while u_c and u_l denote the volume fractions of PC and limestone powder particles in the total solid particles. Additionally, the solid particle packing density of PC-limestone paste is determined by Eq. (2.3):

$$\text{(2.3)} \qquad \varphi = \frac{1}{1 + \rho_m \dfrac{m_w}{m_b}}$$

where, ρ_m signifies the density of the mixed powder of cement and limestone powder (kg/m^3), m_w is the water requirement when the paste achieves the standard consistency (kg), and m_b represents the mass of the binder material (kg). The minimum water requirement is determined based on the critical water consumption for the transformation of powder materials from a solid to a paste. ρ_m can be approximated calculated using Eq. (2.4):

$$\text{(2.4)} \qquad \rho_m = \frac{m_c}{m_b}\rho_c + \frac{m_l}{m_b}\rho_l$$

where, m_c and m_l are the masses of PC and limestone powder, respectively, ρ_c and ρ_l is the density of cement and limestone powder (kg/m^3), respectively. Finally, the WFT of the paste can be determined by Eq. (2.5), where u_w' is the ratio of excess water to solid particle volume

(excess water ratio); u_w is the ratio of water volume to solid particle volume, and u_{void} is the ratio of void volume to solid particle volume [40].

$$(2.5) \qquad \text{WFT} = \frac{u'_w}{\text{TSSA}} = \frac{u_w - u_{\text{void}}}{\text{TSSA}} = \frac{u_w - \dfrac{1-\varphi}{\varphi}}{\text{TSSA}}$$

3. Results and discussion

3.1. Dynamic yield stress

Figure 2 illustrates the impact of varying limestone powder content on the flow curve of the composite paste. The relationship between shear stress and shear rate was modeled using the modified Bingham model to determine the dynamic yield stress for each set of slurries. The inclusion of a quadratic coefficient in the modified Bingham model accounts for the nonlinear characteristics of the flow curve, accommodating potential shear thickening or shear thinning in the slurry. Observing Fig. 2, it becomes apparent that the shear stress of the slurry without added limestone powder exhibits a nearly linear variation with shear rate, resulting in a smaller quadratic coefficient compared to other groups. As the limestone powder dosage increases, the shear stress of the slurry begins to ascend, indicating a transition in rheological properties towards shear thickening, signified by an increase in the ratio of shear stress to shear rate (apparent viscosity).
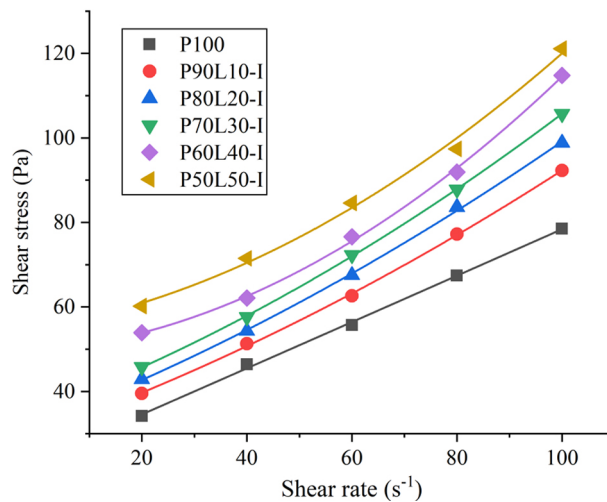

Fig. 2. Shear stress-shear rate relationships of PC-limestone pastes

To further quantify the dynamic yield stress for each group of slurries, Table 2 presents the fitting equations for the 16 groups investigated in this study. Notably, the fitting accuracy across all slurries is consistently high, with R^2 values predominantly reaching 0.99 or above.

Irrespective of the specific surface area of the limestone powder, the dynamic yield stress of the slurry steadily rises with increasing limestone powder content. Moreover, when limestone powder dosage is uniform, limestone powder with a larger specific surface area induces a more pronounced increase in yield stress. For instance, the dynamic yield stress of the slurry containing 50% Class I limestone powder (with a specific surface area of 389 m²/kg) is measured at 54.9 Pa, while the slurry containing Class III limestone powder (1088 m²/kg) at a 50% substitution rate exhibits a notably higher dynamic yield stress of 70.26 Pa.

Table 2. Fitting parameters based on the modified Bingham model

Sample	Modified Bingham model	R^2	Dynamic yield stress
P100	$\tau = 0.000036\gamma^2 + 0.5437\gamma + 23.66$	0.9975	23.66
P90L10-I	$\tau = 0.0017\gamma^2 + 0.4454\gamma + 30.08$	0.9991	30.08
P80L20-I	$\tau = 0.0019\gamma^2 + 0.4805\gamma + 32.34$	0.9989	32.34
P70L30-I	$\tau = 0.0023\gamma^2 + 0.4714\gamma + 35.31$	0.9998	35.31
P60L40-I	$\tau = 0.0054\gamma^2 + 0.1109\gamma + 49.48$	0.9980	49.48
P50L50-I	$\tau = 0.0044\gamma^2 + 0.2135\gamma + 54.9$	0.9903	54.9
P90L10-II	$\tau = 0.00021\gamma^2 + 0.4325\gamma + 32.56$	0.9912	32.56
P80L20-II	$\tau = 0.00052\gamma^2 + 0.3754\gamma + 36.59$	0.9889	36.59
P70L30-II	$\tau = 0.0016\gamma^2 + 0.3298\gamma + 45.25$	0.9992	45.25
P60L40-II	$\tau = 0.0014\gamma^2 + 0.3194\gamma + 51.22$	0.9978	51.22
P50L50-II	$\tau = 0.0025\gamma^2 + 0.2016\gamma + 57.85$	0.9991	57.85
P90L10-III	$\tau = 0.00046\gamma^2 + 0.3978\gamma + 35.33$	0.9975	35.33
P80L20-III	$\tau = 0.0011\gamma^2 + 0.3426\gamma + 40.71$	0.9981	40.71
P70L30-III	$\tau = 0.0017\gamma^2 + 0.2012\gamma + 49.97$	0.9966	49.97
P60L40-III	$\tau = 0.0021\gamma^2 + 0.2345\gamma + 58.62$	0.9979	58.62
P50L50-III	$\tau = 0.002\gamma^2 + 0.2102\gamma + 70.26$	0.9965	70.26

3.2. Static yield stress

In contrast to dynamic yield stress, static yield stress characterizes the stress required to sustain the flow of the slurry [7, 18]. The progression of stress under low shear rates is depicted in Figs. 3 and 4, illustrating a rapid initial ascent followed by a gradual decline and stabilization. This pattern aligns with the solid-liquid transition observed in the slurry, where shear forces induce microstructural damage, leading to a shift from a solid state dominated by elasticity to a liquid state characterized by viscosity.

Based on the results obtained from Figs. 3 and 4, Fig. 5 amalgamates the maximum stress, denoting static yield stress, across each set of slurries throughout the testing duration. In concordance with the dynamics of dynamic yield stress, both the addition of limestone powder and the augmentation of its specific surface area contribute to an elevation in the static yield stress of the slurry. Notably, static yield stress appears to undergo a more pronounced increase compared to dynamic yield stress, as evident from the integrated results in Fig. 5.
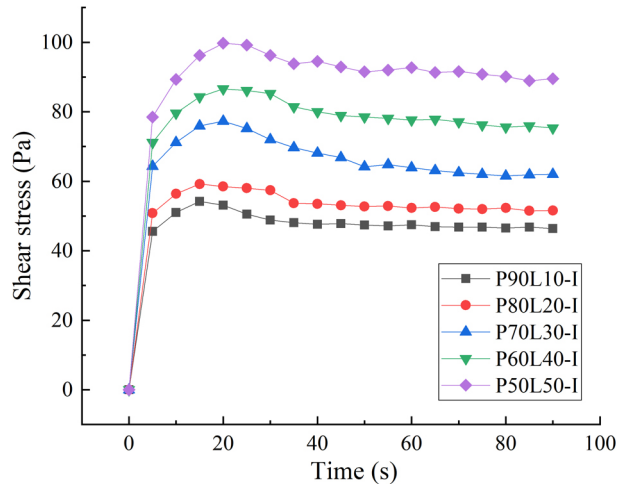
Fig. 3. Effect of limestone content on static yield stress of composite pastes
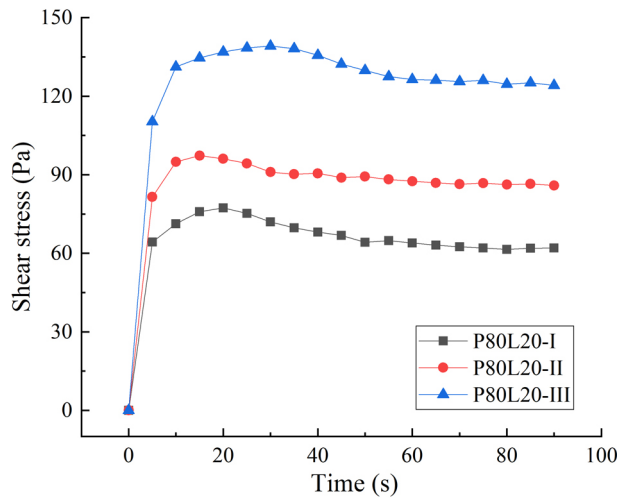
Fig. 4. Effect of particle size of limestone on static yield stress of composite pastes
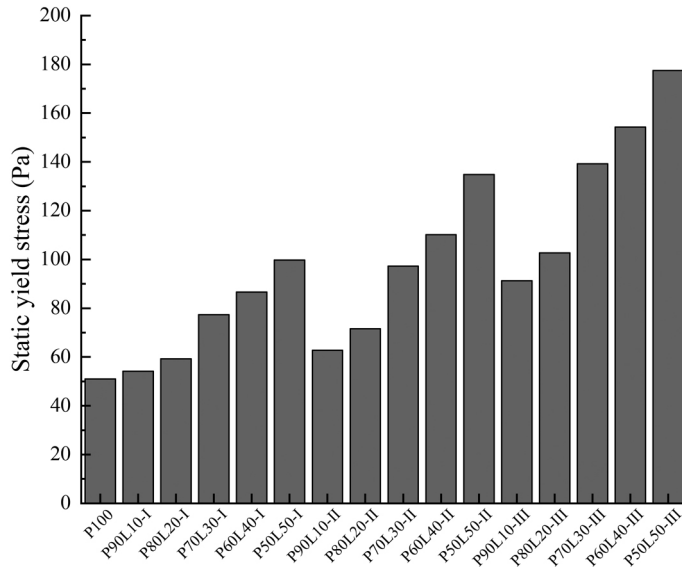
Fig. 5. Static yield stress of PC-limestone pastes

3.3. Water film thickness

Upon computing the WFT for each set of slurries, Fig. 6 scrutinizes the influence of $\varphi/TSSA$ on WFT. As depicted, there exists an approximate quadratic growth relationship between $\varphi/TSSA$ and WFT. As per Eq. (2.5), WFT represents the ratio of excess water in solid
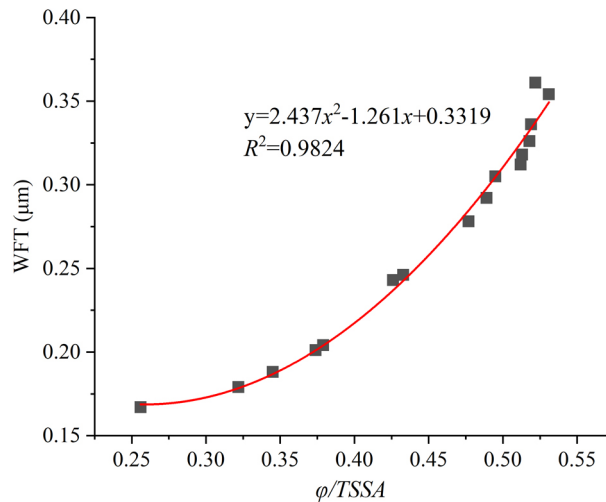
Fig. 6. Effect of $\varphi/TSSA$ on WFT of PC-limestone paste

particles to the total specific surface area. The escalation in total specific surface area exerts a diminishing impact on water film thickness, while the proportion of excess water exerts an elevating effect on WFT. Consequently, the value of WFT hinges on the relative magnitude of these two parameters. Results from Fig. 6 indicate that a higher ratio of solid particle packing density to total specific surface area corresponds to a greater WFT in composite slurry. Moreover, an increase in the current ratio intensifies the growth of WFT.

From a dynamic standpoint, the variation in water film thickness among different cement limestone powder slurries results from the combined influence of solid particle packing density and total specific surface area. To delve deeper into how WFT affects the yield stress of composite slurries, Figs. 7 and 8 illustrate the relationship between the two types of yield stresses and WFT. It is evident that both yield stresses exhibit a negative correlation with WFT, implying that an augmentation in WFT precipitates a reduction in yield stress. The heightened thickness of lubricating water on particle surfaces, accompanying an increase in WFT, diminishes friction between particles. However, a nuanced functional relationship is apparent: dynamic yield stress approximates a linear decrease, whereas static yield stress demonstrates a decrease in an inverse proportional function. This distinction may arise from the fact that, at small WFT values, particles tend to accumulate more readily, forming early microstructures that necessitate greater external forces to disrupt and facilitate slurry flow. Consequently, the static yield stress of slurry with smaller WFT significantly surpasses that of slurry with larger WFT.

3.4. Prediction of yield stress based on WFT

Although Figs. 7 and 8 can demonstrate the relationship between the yield stress of the slurry and WFT, this relationship is more of a regular description. It is difficult to achieve the goal of accurately characterizing the yield stress of the slurry through this simple fitting. Therefore, this study also employed the currently popular machine learning approach to attempt to predict the yield stress of the slurry through mix ratio parameters and WFT.

Artificial neural networks (ANN) are currently the most widely used and reliable machine learning algorithms. It mainly consists of three parts: input layer, hidden layer, and output layer. In this study, the activation function adopts the sigmoid function, as shown in Eq. (3.1):

$$(3.1) \qquad s(x) = \frac{1}{1 + e^{-x}}$$

In addition, the weights and thresholds of the network are adjusted by transferring the error function in the opposite direction to achieve the goal of minimizing errors as much as possible. The expression is shown in Eq. (3.2), where T_i is the expected output and O_i is the calculated output of the network.

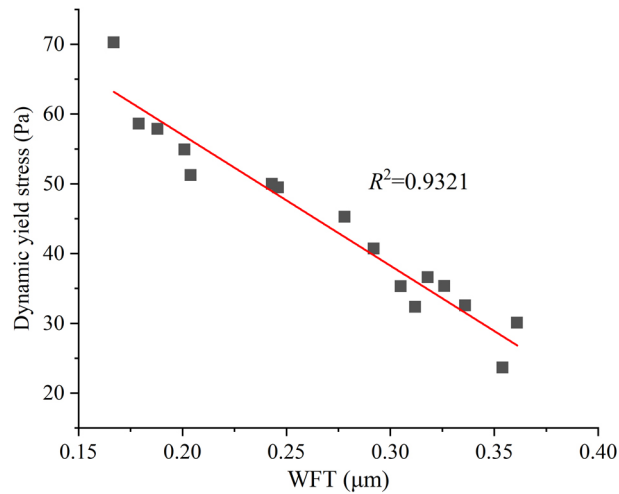$$(3.2) \qquad E = \frac{\sum_i (T_i + O_i)^2}{2}$$

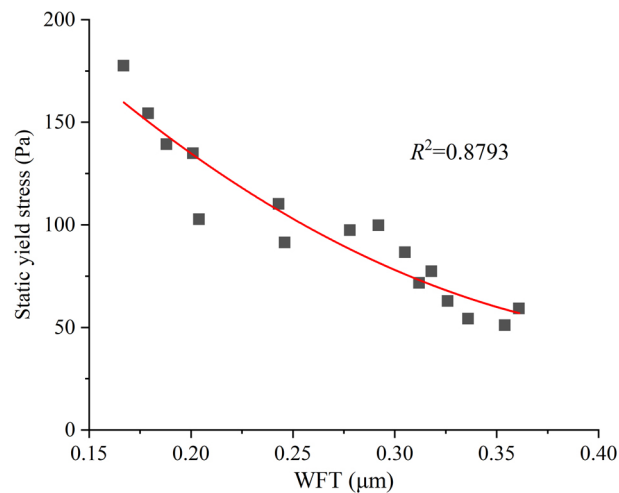Fig. 7. Relationship between WFT and Dynamic yield stress

Fig. 8. Relationship between WFT and Dynamic yield stress

In this study, input parameters include PC percentage content (50–100%), limestone powder percentage content (0–50%), and WFT. The prediction of artificial neural networks mainly involves the following main processes:

(i) Divide the data into training and testing sets in a ratio of 80% and 20%, and normalize all input parameters.

(ii) Determine the number of hidden layers. Here we refer to the empirical formula previously proposed, as shown in Eq. (3.3):

$$(3.3) \qquad\qquad l = \sqrt{n + m} + a$$

where, n is the number of input layers, m is the number of output layers, and a is a constant between 1 and 10. Based on the background of this study, the hidden layer was determined to be 5.

(iii) Implement network training and data prediction through Matlab 2019a.

The prediction results of dynamic and static yield stress of PC limestone powder composite slurry based on artificial neural network prediction are shown in Fig. 9. It can be found that using machine learning methods can obtain results more accurately than traditional simple fitting methods. This can be mainly reflected by the fact that both the predicted and actual values are almost evenly distributed on both sides of the red line in Fig. 9. However, compared to static yield stress (Fig. 9(a)), the accuracy of predicting dynamic yield stress values is relatively lower.
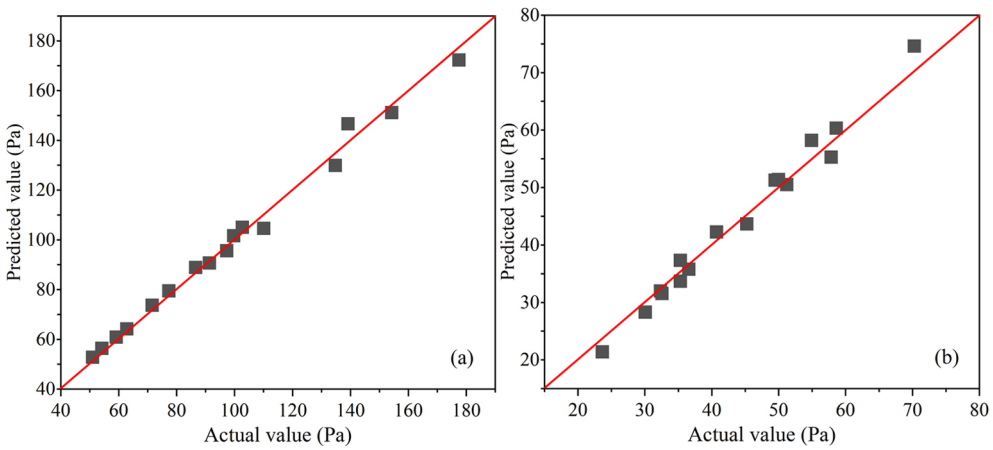
Fig. 9. Actual yield stress and Predicted yield stress showing (a) static yield stress and (b) dynamic yield stress

Figure 9 is only a visual comparison between predicted and actual values, rather than a rigorous quantification. In order to further evaluate the difference between the predicted and actual values, i.e. the overall deviation of the sample, the determination coefficient R^2 is used to evaluate the performance of the given model. The calculation method for R^2 is given by Eq. (3.4), where y_i' is the predicted value and y_i is the actual value.

$$(3.4) \qquad R^2 = 1 - \frac{\sum_{i=1}^{n} \left(y_i' - y_i \right)^2}{\sum_{i=1}^{n} (y_i - \bar{y})^2}$$

Figure 10 shows the prediction accuracy characterization results of an R^2-based artificial neural network. It can be found that the accuracy of using this algorithm to predict two types of yield stresses exceeds 0.94, with the accuracy of predicting static yield stresses reaching as high as 0.9745. This once again demonstrates that using artificial neural networks, a more

advanced algorithm, can more accurately obtain the yield stress of the slurry than empirical models. Moreover, based on the results in Fig. 9, it can be observed that the prediction process did not exhibit the overfitting phenomenon that is commonly observed in machine learning models. In other words, both the training and testing sets exhibit good predictive accuracy.
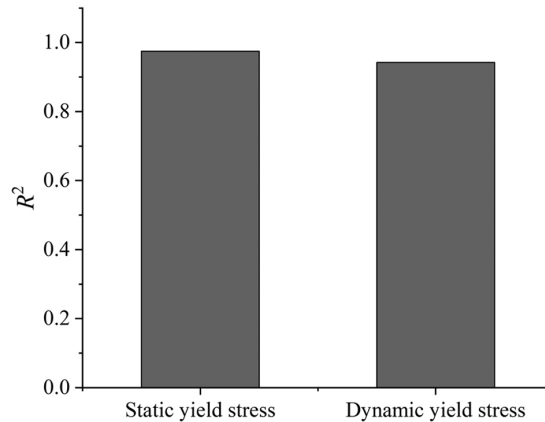

Fig. 10. R^2 of static and dynamic yield stresses

4. Conclusions

This study integrates particle packing theory to establish the correlation between WFT and yield stress in PC-limestone paste. Additionally, a state-of-the-art artificial neural network were employed to predict yield stress. The principal conclusions are summarized as follows:

1. The shear stress-shear rate relationship of PC-limestone paste demonstrates an approximate linear growth pattern. As limestone powder content increases, the paste's shear thickening intensifies. The addition of limestone powder, coupled with an augmentation in specific surface area, markedly amplifies the static and dynamic yield stress of the paste. Notably, the dynamic yield stress for paste with 50% Class III limestone powder (1088 m^2/kg) reaches 70.26 Pa.

2. WFT in PC-limestone paste particles is influenced by the ratio of solid particle packing density to total specific surface area, increasing with higher solid particle packing density. Both dynamic and static yield stresses exhibit negative correlations with WFT, signifying that an increase in WFT corresponds to a decrease in yield stress. The dynamic yield stress demonstrates an approximate linear decrease with WFT, while the static yield stress manifests a decrease following an inverse proportional function.

3. Artificial neural networks are proficient in predicting static and dynamic yield stresses based on mix ratio parameters and WFT. Significantly, static yield stress prediction accuracy is higher, with an R^2 value of 0.9745. The application of the artificial neural algorithm provides a crucial computational foundation for establishing a rational relationship between WFT and yield stress.

References

[1] Y. Zhang, X. Kong, L. Gao, Z. Lu, S. Zhou, B. Dong, and F. Xing, "In-situ measurement of viscoelastic properties of fresh cement paste by a microrheology analyzer", *Cement and Concrete Research*, vol. 79, pp. 291–300, 2016, doi: 10.1016/j.cemconres.2015.09.020.

[2] Y. Guo, T. Zhang, J. Wei, Q. Yu, and S. Ouyang, "Evaluating the distance between particles in fresh cement paste based on the yield stress and particle size", *Construction and Building Materials*, vol. 142, pp. 109–116, 2017, doi: 10.1016/j.conbuildmat.2017.03.055.

[3] N. Roussel, H. Bessaies-Bey, S. Kawashima, D. Marchon, K. Vasilic, and R. Wolfs, "Recent advances on yield stress and elasticity of fresh cement-based materials", *Cement and Concrete Research*, vol. 124, art. no. 105798, 2019, doi: 10.1016/j.cemconres.2019.105798.

[4] J. Mzwandile, M. Willy, and H. Rainer, "Cement paste yield stress and self-compacting mortar stability", *Construction and Building Materials*, vol. 393, art. no. 131917, 2023, doi: 10.1016/j.conbuildmat.2023.131917.

[5] Y. Chen, Y. Zhang, B. Šavija, and O. Çopuroğlu, "Fresh properties of limestone-calcined clay-slag cement pastes", *Cement and Concrete Composites*, vol. 138, art. no. 104962, 2023, doi: 10.1016/j.cemconcomp.2023.104962.

[6] K. Fang, D. Zhang, D. Wang, Z. Liu, M. Zhang, and S. Zhang, "The impact of coal gasification slag powder on fluidity, rheology and viscoelasticity properties of fresh cement paste", *Journal of Building Engineering*, vol. 69, art. no. 106237, 2023, doi: 10.1016/j.jobe.2023.106237.

[7] Y. Qian and S. Kawashima, "Distinguishing dynamic and static yield stress of fresh cement mortars through thixotropy", *Cement and Concrete Composites*, vol. 86, pp. 288–296, 2018, doi: 10.1016/j.cemconcomp.2017.11.019.

[8] Y. Peng and C. Unluer, "Advances in rheological measurement and characterization of fresh cement pastes", *Powder Technology*, vol. 429, art. no. 118903, 2023, doi: 10.1016/j.powtec.2023.118903.

[9] T. Wangler, N. Roussel, F.P. Bos, T.A. Salet, and R.J. Flatt, "Digital concrete: a review", *Cement and Concrete Research*, vol. 123, art. no. 105780, 2019, doi: 10.1016/j.cemconres.2019.105780.

[10] A.R. Arunothayan, B. Nematollahi, K.H. Khayat, A. Ramesh, and J.G. Sanjayan, "Rheological characterization of ultra-high performance concrete for 3D printing", *Cement and Concrete Composites*, vol. 136, art. no. 104854, 2023, doi: 10.1016/j.cemconcomp.2022.104854.

[11] S. Paritala, K.K. Singaram, I. Bathina, M.A. Khan, and S.K.R. Jyosyula, "Rheology and pumpability of mix suitable for extrusion-based concrete 3D printing–A review", *Construction and Building Materials*, vol. 402, art. no. 132962, 2023, doi: 10.1016/j.conbuildmat.2023.132962.

[12] J. Xiao, S. Hou, Z. Duan, and S. Zou, "Rheology of 3D printable concrete prepared by secondary mixing of ready-mix concrete", *Cement and Concrete Composites*, vol. 138, art. no. 104958, 2023, doi: 10.1016/j.cemconcomp.2023.104958.

[13] Y. Peng and C. Unluer, "Development of alternative cementitious binders for 3D printing applications: A critical review of progress, advantages and challenges", *Composites Part B: Engineering*, vol. 252, art. no. 110492, 2023, doi: 10.1016/j.compositesb.2022.110492.

[14] L. Tang, Z. Wang, X. Zhang, X. Chen, J. Luo, and Y. Wang, "Influence of rheological parameters on cement slurry penetration characteristics of novel oscillating grouting technology", *Construction and Building Materials*, vol. 409, art. no. 133999, 2023, doi: 10.1016/j.conbuildmat.2023.133999.

[15] J. Shi, Y. Liu, H. Xu, Y. Peng, Q. Yuan, and J. Gao, "The roles of cenosphere in ultra-lightweight foamed geopolymer concrete (UFGC)", *Ceramics International*, vol. 48, no. 9, pp. 12884–12896, 2022, doi: 10.1016/j.ceramint.2022.01.161.

[16] T. Liberto, M. Bellotto, and A. Robisson, "Small oscillatory rheology and cementitious particle interactions", *Cement and Concrete Research*, vol. 157, art. no. 106790, 2022, doi: 10.1016/j.cemconres.2022.106790.

[17] Q. Yuan, D. Zhou, K. H. Khayat, D. Feys, and C. Shi, "On the measurement of evolution of structural build-up of cement paste with time by static yield stress test vs. small amplitude oscillatory shear test", *Cement and Concrete Research*, vol. 99, pp. 183–189, 2017, doi: 10.1016/j.cemconres.2017.05.014.

[18] Y. Peng and C. Unluer, "Investigation of the viscoelastic evolution of reactive magnesia cement pastes with accelerated hydration mechanisms", *Cement and Concrete Composites*, vol. 142, art. no. 105191, 2023, doi: 10.1016/j.cemconcomp.2023.105191.

[19] N. Roussel, G. Ovarlez, S. Garrault, and C. Brumaud, "The origins of thixotropy of fresh cement pastes", *Cement and Concrete Research*, vol. 42, no. 1, pp. 148–157, 2012, doi: 10.1016/j.cemconres.2011.09.004.

[20] R.J. Flatt, N. Roussel, H. Bessaies-Bey, L. Caneda-Martínez, M. Palacios, and F. Zunino, "From physics to chemistry of fresh blended cements", *Cement and Concrete Research*, vol. 172, art. no. 107243, 2023, doi: 10.1016/j.cemconres.2023.107243.

[21] B.S. Thomas, "Green concrete partially comprised of rice husk ash as a supplementary cementitious material–A comprehensive review", *Renewable and Sustainable Energy Reviews*, vol. 82, pp. 3913–3923, 2018, doi: 10.1016/j.rser.2017.10.081.

[22] Y. Nie, J. Shi, Z. He, B. Zhang, Y. Peng, and J. Lu, "Evaluation of high-volume fly ash (HVFA) concrete modified by metakaolin: Technical, economic and environmental analysis", *Powder Technology*, vol. 397, art. no. 117121, 2022, doi: 10.1016/j.powtec.2022.117121.

[23] Y. Peng and C. Unluer, "Modeling the mechanical properties of recycled aggregate concrete using hybrid machine learning algorithms", *Resources, Conservation and Recycling*, vol. 190, art. no. 106812, 2023, doi: 10.1016/j.resconrec.2022.106812.

[24] N. Nie, "Prediction of concrete life under coupled dry and wet-sulfate erosion based on damage evolution equation", *Archives of Civil Engineering*, vol. 69, no. 4, pp. 679–692, 2023, doi: 10.24425/ace.2023.147683.

[25] S. Her, T. Park, E. Zalnezhad, and S. Bae, "Synthesis and characterization of cement clinker using recycled pulverized oyster and scallop shell as limestone substitutes", *Journal of Cleaner Production*, vol. 278, art. no. 123987, 2021, doi: 10.1016/j.jclepro.2020.123987.

[26] Y. Peng and C. Unluer, "Analyzing the mechanical performance of fly ash-based geopolymer concrete with different machine learning techniques", *Construction and Building Materials*, vol. 316, art. no. 125785, 2022, doi: 10.1016/j.conbuildmat.2021.125785.

[27] K. Kuzmenko, N. Ducoulombier, A. Feraille, and N. Roussel, "Environmental impact of extrusion-based additive manufacturing: generic model, power measurements and influence of printing resolution", *Cement and Concrete Research*, vol. 157, art. no. 106807, 2022, doi: 10.1016/j.cemconres.2022.106807.

[28] A.A. Ramezanianpour, E. Ghiasvand, I. Nickseresht, M. Mahdikhani, and F. Moodi, "Influence of various amounts of limestone powder on performance of Portland limestone cement concretes", *Cement and Concrete Composites*, vol. 31, no. 10, pp. 715–720, 2009, doi: 10.1016/j.cemconcomp.2009.08.003.

[29] D. Wang, C. Shi, N. Farzadnia, Z. Shi, H. Jia, and Z. Ou, "A review on use of limestone powder in cement-based materials: Mechanism, hydration and microstructures", *Construction and Building Materials*, vol. 181, pp. 659–672, 2018, doi: 10.1016/j.conbuildmat.2018.06.075.

[30] B. Lothenbach, G. Le Saout, E. Gallucci, and K. Scrivener, "Influence of limestone on the hydration of Portland cements", *Cement and Concrete Research*, vol. 38, no. 6, pp. 848–860, 2008, doi: 10.1016/j.cemconres.2008.01.002.

[31] J.J. Chen and A.K.H. Kwan, "Superfine cement for improving packing density, rheology and strength of cement paste", *Cement and Concrete Composites*, vol. 34, no. 1, pp. 1–10, 2012, doi: 10.1016/j.cemconcomp.2011.09.006.

[32] Y. Peng, K. Ma, G. Long, Y. Xie, L. Yu, and Q. Xie, "Effect of packing density according to CPM on the rheology of cement–fly ash–slag paste", *Journal of Materials in Civil Engineering*, vol. 33, no. 8, art. no. 04021209, 2021, doi: 10.1061/(ASCE)MT.1943-5533.0003823.

[33] P. Belin, G. Habert, M. Thiery, and N. Roussel, "Cement paste content and water absorption of recycled concrete coarse aggregates", *Materials and Structures*, vol. 47, pp. 1451–1465, 2014, doi: 10.1617/s11527-013-0128-z.

[34] D. Kulisch, A. Katz, and S. Zhutovsky, "Quantification of residual unhydrated cement content in cement pastes as a potential for recovery", *Sustainability*, vol. 15, no. 1, art. no. 263, 2022, doi: 10.3390/su15010263.

[35] V. Rostami, Y. Shao, A.J. Boyd, and Z. He, "Microstructure of cement paste subject to early carbonation curing", *Cement and Concrete Research*, vol. 42, no. 1, pp. 186–193, 2012, doi: 10.1016/j.cemconres.2011.09.010.

[36] W. Li, Y. Xie, K. Ma, G. Long, N. Li, W. Jiang, and Y. Peng, "Microstructure characteristics and evolution of the bonding interface between SCC and steam-cured concrete", *Construction and Building Materials*, vol. 400, art. no. 132837, 2023, doi: 10.1016/j.conbuildmat.2023.132837.

[37] W. Li, Y. Xie, K. Ma, G. Long, H. Zhao, and Y. Peng, "Multiscale mechanical evolution of the interface between self-compacting concrete and steam-cured concrete", *Journal of Building Engineering*, vol. 73, art. no. 106793, 2023, doi: 10.1016/j.jobe.2023.106793.

[38] R. S. Campos and G.F. Maciel, "Test protocol and rheological model influence on determining the rheological properties of cement pastes", *Journal of Building Engineering*, vol. 44, art. no. 103206, 2021, doi: 10.1016/j.jobe.2021.103206.

[39] Y. Jeong, C.W. Hargis, S.C. Chun, and J. Moon, "The effect of water and gypsum content on strätlingite formation in calcium sulfoaluminate-belite cement pastes", *Construction and Building Materials*, vol. 166, pp. 712–722, 2018, doi: 10.1016/j.conbuildmat.2018.01.153.

[40] Q. Li and Y. Fan, "Rheological evaluation of nano-metakaolin cement pastes based on the water film thickness", *Construction and Building Materials*, vol. 324, art. no. 126517, 2022, doi: 10.1016/j.conbuildmat.2022.126517.